The Failure of Wire-Arc Additive Manufactured Aluminum Alloys With Porosities Under Loadings as Observed by In-Situ X-Ray Micro-Computed Tomography

Runyu Zhang*, Yuxin Jiao*, Christopher Paniagua*, Yi Tian*, Hongbing Lu*, and Wei Li*

*Department of Mechanical Engineering, The University of Texas at Dallas, Richardson, TX 75080, USA

Abstract

Wire-arc additive manufactured aluminum alloys (WAAM 4043 Aluminum) are widely used in many industries. Porosities are known to exist within the WAAM aluminum alloys, which greatly reduces the usability and reliability of such parts. In this study, WAAM aluminum alloy samples with porosities are manufactured using a Fronius (TPS 320i) MIG/MAG welding and ABB (IRB 140) robot system. The porosities generated inside the samples and the porosity evolution under the uniaxial tension are observed using in-situ X-ray micro-computed tomography (μCT). The μCT system with an integrated mechanical loading frame provides in-situ volumetric images of the specimens while loadings are applied. The porosity evolution of the WAAM aluminum samples and the propagation of the internal pores are assessed. This work provides direct experimental observations and evaluations of the influence of porosities on the mechanical behavior of WAAM aluminum alloys under loadings.

Keywords: Wire-arc additive manufacturing (WAAM), porosity propagation, in-situ X-ray micro-computed tomography (μCT)

Introduction

Wire arc additive manufacturing (WAAM) is the process of combining the gas metal arc welding (GMAW) process with additive manufacturing (AM), that the metal wire is melted as feedstock using the high-power electric arc to form the geometry and the parts with designated printing path. Compared to the power-based AM process, the WAAM process has a significantly lower cost, better applicability to reflective metals, and is also more environmental-friendly [1]. However, like any other AM process, processing parameters directly influence the printing process, including microstructure evolutions [2,3], molten pool formations [4,5], etc., thus determining the quality of the printed parts. Porosities are known to be the primary defects in the aluminum WAAM parts, due to significant solubility differences of hydrogen in aluminum liquid and solid [6,7]. Postprocessing is often applied to mitigate and reduce porosity formed in the parts [8,9], however, their mechanical properties are still often compromised [10]. In this study, single-track and multi-layer aluminum WAAM samples are printed with different processing parameters, and the porosity generation and evolution under uniaxial tension are studied using an in-situ X-ray micro-computed tomography (μCT) system. The volumetric images from the reconstructed μCT provide direct experimental observations of the porosity size and distribution inside the WAAM prints from different processing parameters, and the porosity evolution under loading can be used to validate simulations in the future study.

Materials and Methods

All single-track and multi-layer samples are prepared using the WAAM system of the ABB robot arm and Fronius welder as shown in figure 1(a). The motion control platform for this WAAM process is a programable ABB robot arm that allows for six degrees of motion. This platform allows for accurate tool positioning when working in a small area. A Fronius TPS 320ti is used to set the welding parameters of the WAAM process, and the main factors consist of the current (A) and voltage applied, the wire feed rate (WFS) (mm/min), and the inert gas flow rate (CFH). One feature of the Fronius TPS 320ti system is selecting "wall thickness", a setting for traditional MIG welding, by changing which the system current, voltage, and WFR are automatically adjusted. To observe the porosities inside the WAAM samples and the porosity evolution during the uniaxial tension, a Nikon 225 kV X-ray μCT system with an integrated mechanical loading frame (Psylotech, Evanston, IL) as shown in figure 1(b) is used. The X-ray μCT system is able to image the samples with voxel size up to 3 μm/voxel while applying the load to reveal the interior of the samples under loading, and such in-situ X-ray μCT systems have been used in many applications for characterizing materials properties [11–13], and real-time monitoring in additive manufacturing [14,15].
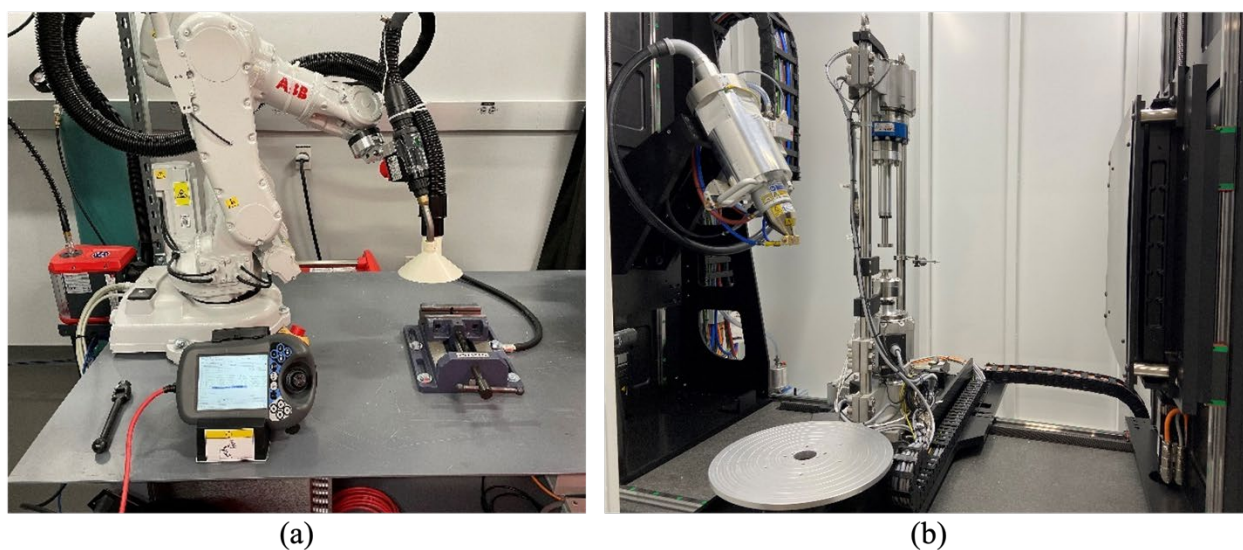

| (a) | (b) |

Fig. 1 Equipment used in this study (a) The WAAM system of ABB robot arm and Fronius welder, and (b) a Nikon in-situ X-ray μCT system with a loading frame.

All WAAM samples are printed on aluminum substrates cut to 25.60 mm x 50.40 mm x 12.80 mm. Preparation of the substrates consists of deburring after cutting to fit in the vice grip and a cleaned before printing began. Cleaning was done with a steel brush, acetone, and IPA ultrasonication for 5 minutes after the substrates were dried before printing. The printing material is a commercial wire filler of Al 4043 manufactured by Forney. All multi and single-layer prints used the Fronius MIG pulse power source as their arc mode. The deposition strategy consists of hatching between layers to maintain uniform layering. All individual printing tacks of each sample kept consistent WFS/TS ratio, welding intensity, shielding gas flow rate (31.20 CFH) of pure argon, and working tip distance to the substrate at 10 mm. Different scanning patterns and WFS/TS ratios were conducted between samples to obtain uniform geometry prints. All samples were

preheated to 45 – 55 C by a heat gun and measured by a FLIR E5-XT infrared camera. Once the substrate was brought up to temperature, a single track was deposited and then cleaned with a steel brush with a 90-second dwell time. The nozzle was moved two-thirds of the track width and deposited in the same direction, followed by the same cleaning and dwell time. The same printing process is repeated for multi-layer prints.

Table 1 Tested Fronius wall thickness presetting and the corresponding printing parameters

Parameters	Fronius wall thickness presetting (inch)			
	0.10	0.16	0.20	0.50
Current (A)	81	124	153	241
Voltage (V)	17.7	19.6	21.3	25.2
Power (W)	1433.7	2430.4	3258.9	6073.2
Wire feeding speed (inch/minute)	270	400	480	750

Table 2 Printing parameters of multi-layer WAAM aluminum samples

	Wall thickness (inch)	Printing speed (mm/s)	Shielding gas flow rate (CFH)	Line width movement (mm)	Height movement (mm)	Tracks / layer	Number of layers
1	0.50	8	31.2	-	-	1	1
2	0.20	8	31.2	-	-	1	1
3	0.16	8	31.2	-	-	1	1
4	0.10	8	31.2	-	-	1	1
5	0.20	15	31.2	4	2	3	6
6	0.20	6	31.2	6	3	2	3
7	0.20	6	31.2	7	3	2	3
8	0.20	8	31.2	6	3	2	4

As there are many parameters to adjust and optimize in WAAM, and the time and cost investment would be significant if each parameter were explored, the Fronius intelligent welding process is utilized to simplify the printing parameters. The primary parameter studied for the optimum printing is the printing power, and with different "wall thickness" parameters selected, four single-track WAAM samples are prepared as shown in table 2. Both single-layer prints and multiple-layer prints are prepared; only a wall thickness of 0.20 inches is studied with varying printing speeds and print geometries for both printing parameters, as shown in table 2 for multi-layer and single-layer prints. A few factors are considered when designing the printing parameters, such as the wire feeding speed (WFS) over the traveling/printing speed (TS), the WFS/TS ratio, and heat input for temperature control. It is recommended that a WFS/TS ratio of 5 to 25 should

be maintained for an acceptable wall print [4]. For a stable deposition rate and suitable print geometries, the WFS/TS ratio of 13 to 25 is held, and a temperature range of 45 to 55 °C is maintained before printing another track [8].

Result and Discussion

The reconstructed µCT of the four single-track samples are presented in figure 2, including samples 1 to 4, with printing parameters shown in table 2. As the input power increases from setting the wall thickness value at 0.1 inch in figure 2(a), to 0.5 inch in figure 2(d), the number of pores is increasing and larger individual pores are observed. Also, underpower while printing samples 3 and 4 in table 2 leads to surface unevenness and insufficient wire melt, as figures 2(a) and (b) show; whereas the excessive power input causes sample collapse and over-melting of the substrate as figure 2(d) shows. Therefore, from the preliminary study of printing single-track WAAM samples to obtain the optimized input power, the presetting "wall thickness" of 0.2 inch with a current of 153 A, a voltage of 21.3 V, and wire feeding speed of 480 inch/minute is selected for printing multi-layer samples.
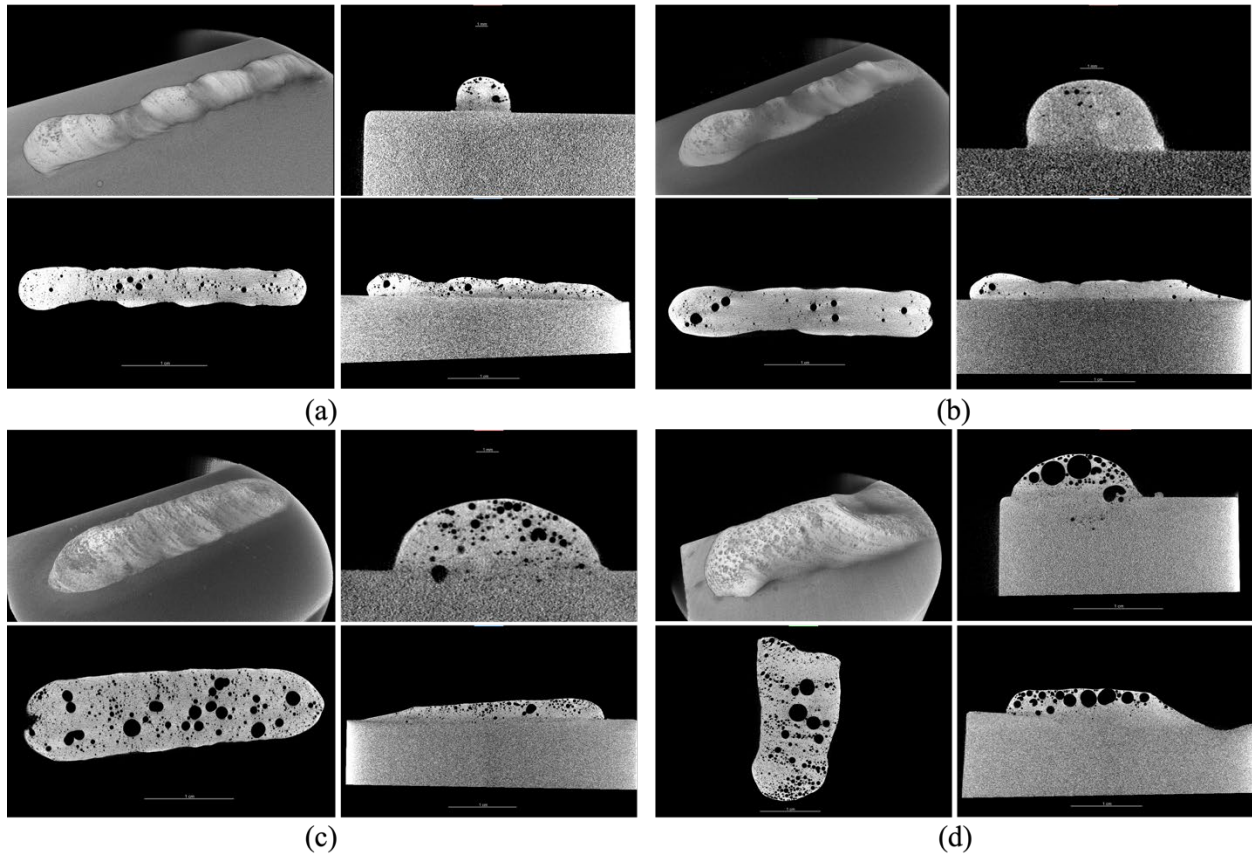

(a)

(b)

(c)

(d)

Fig. 2 The reconstructed X-ray µCT of four single-track WAAM samples showing the three cross sections and the 3D rendering, including (a) sample 4, (b) sample 3, (c) sample 2, and (d) sample 1, as shown in table 2.

Four multi-layer WAAM samples are manufactured using the processing parameters listed as "sample 5" to "samples 8" in table 2, and then cut into a cylindrical

shape with a length of 30 mm and a diameter of 10 mm using a wire electrical discharge machine (EDM). All four samples are imaged using the X-ray µCT system to inspect the porosity inside as shown in figure 3. Based on printing parameters listed in table 2, all four samples are manufactured with the same input power and shielding gas flow rate, whereas the printing speed, the number of tracks per layer, and the total number of layers vary. From µCT images in figure 3, there is significantly less amount of porosity inside sample 5 compared to the other three, which indicates that a travel speed of 15 mm/s is the optimum value in the study. Although sample 5 is printed with the largest number of tracks per layer and the most number of layers in total among all four samples, it is often believed that the travel speed is the most influential factor among all three parameters here in determining the quality of WAAM parts, due to its impact on the input power into the system, the molten pool formation, liquid solidification rate, etc. [1,4,6,7,15].
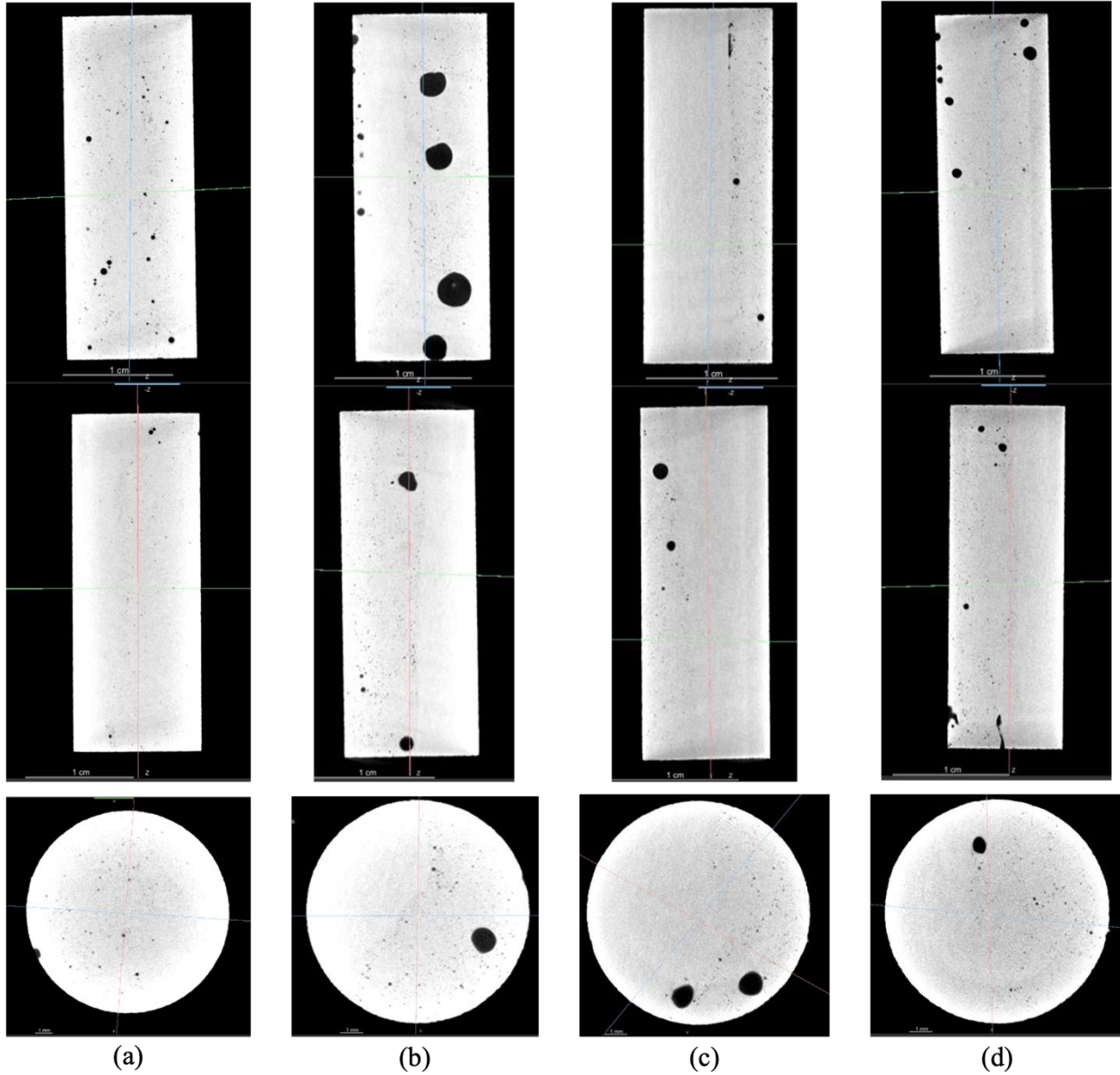
Fig. 3 Cross-sectional view of the reconstructed X-ray μCT of four multi-layer WAAM samples, including (a) sample 5, (b) sample 6, (c) sample 7, and (d) sample 8, as shown in table 2.
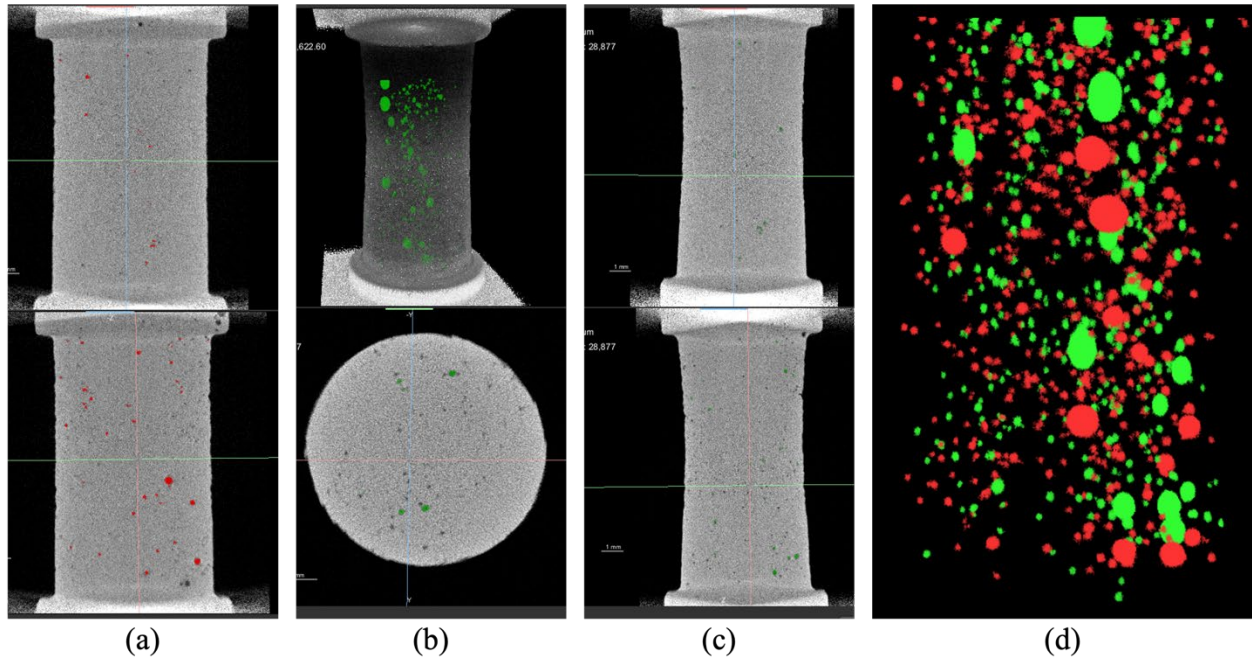
Fig. 4 The reconstructed μCT showing the sample and the porosity inside (a) at the intact state, (b) and (c) at the loaded state under uniaxial tension, and (d) the porosity evolution before and during the uniaxial tension loading.

To observe the porosity evolution in the WAAM sample, the center portion of sample 5 is further lathed to a reduced section with a gauge length of 10 mm and a diameter of 6 mm, and then the lathed sample is loaded with a uniaxial tension on the in-situ X-ray μCT machine. The sample in the intact state and loaded state are imaged, and the reconstructed μCT is shown in figure 4. All porosities are segmented from the μCT using Otsu's method based on the grayscale value, with a minimum pore diameter of 100 μm as the threshold, as pores with a diameter larger than 100 μm are often considered as the big and inhomogeneously distributed process pores [6,8], and of interest in this study. As figure 4(d) indicates, where the pores at intact and loaded states are marked in red and green, respectively, pores are elongated from a relatively uniform spherical shape into an ellipsoidal shape. And the volume fraction of those pores over the entire porosity inside the sample (excluding pores with diameters smaller than 28.6 μm) at the intact state and loaded state are determined to be 40.2% and 67.8%, respectively. This value suggests that smaller pores form into bigger pores during the uniaxial tension, likely due to voids coalescence and cavity growth.

Conclusion

Experiments on printing WAAM samples with different processing parameters are conducted to explore the porosity generation primarily influenced by the input power and printing speed. And the porosity evolution under uniaxial tension is studied using an in-situ X-ray μCT system. It is found that upon tensile loading, the volume fraction of large pores with diameters larger than 100 μm over the entire porosity inside the sample increases dramatically from 40.2% to 67.8%, due to voids elongation, nucleation, and

coalescence. This study provides insight into the porosity formation and evolution inside the WAAM samples under the uniaxial loading, and is valuable for validating simulation models in future studies.

Acknowledgments

References

[1]   B. Wu, Z. Pan, D. Ding, D. Cuiuri, H. Li, J. Xu, J. Norrish, A review of the wire arc additive manufacturing of metals: properties, defects and quality improvement, Journal of Manufacturing Processes. 35 (2018) 127–139. https://doi.org/10.1016/J.JMAPRO.2018.08.001.

[2]   M. Seifi, A. Salem, D. Satko, J. Shaffer, J.J. Lewandowski, Defect distribution and microstructure heterogeneity effects on fracture resistance and fatigue behavior of EBM Ti–6Al–4V, International Journal of Fatigue. 94 (2017) 263–287. https://doi.org/10.1016/J.IJFATIGUE.2016.06.001.

[3]   W. Li, MODELING AND EXPERIMENTAL INVESTIGATIONS ON PARTICLE DYNAMIC BEHAVIORS IN LASER 3D PRINTING WITH BLOWN POWDER, (n.d.).

[4]   K.F. Ayarkwa, S. Williams, J. Ding, Investigation of pulse advance cold metal transfer on aluminium wire arc additive manufacturing, International Journal of Rapid Manufacturing. 5 (2015) 44. https://doi.org/10.1504/IJRAPIDM.2015.073547.

[5]   R. Zhang, N. Bian, H. Lu, Y. Li, Y. Tian, W. Li, Molten pool swing in printing the steel/inconel functionally gradient material with laser-based Directed Energy Deposition, Manufacturing Letters. 32 (2022) 44–48. https://doi.org/10.1016/J.MFGLET.2022.03.002.

[6]   T. Hauser, R.T. Reisch, P.P. Breese, B.S. Lutz, M. Pantano, Y. Nalam, K. Bela, T. Kamps, J. Volpp, A.F.H. Kaplan, Porosity in wire arc additive manufacturing of aluminium alloys, Additive Manufacturing. 41 (2021) 101993. https://doi.org/10.1016/J.ADDMA.2021.101993.

[7]   M. Arana, E. Ukar, I. Rodriguez, A. Iturrioz, P. Alvarez, Strategies to Reduce Porosity in Al-Mg WAAM Parts and Their Impact on Mechanical Properties, Metals 2021, Vol. 11, Page 524. 11 (2021) 524. https://doi.org/10.3390/MET11030524.

[8]   J. Gu, J. Ding, S.W. Williams, H. Gu, P. Ma, Y. Zhai, The effect of inter-layer cold working and post-deposition heat treatment on porosity in additively manufactured aluminum alloys, Journal of Materials Processing Technology. 230 (2016) 26–34. https://doi.org/10.1016/J.JMATPROTEC.2015.11.006.

[9]   R. Zhang, K.M. Nagaraja, N. Bian, E. Fisher, S. Ahmadyar, K. Bayazitoglu, H. Lu, W. Li, Experimental studies on fabricating functionally gradient material of stainless steel 316L-Inconel 718 through hybrid manufacturing: directed energy

deposition and machining, International Journal of Advanced Manufacturing Technology. 120 (2022) 7815–7826. https://doi.org/10.1007/S00170-022-09304-Y/FIGURES/9.

[10] J.J. Lewandowski, M. Seifi, Metal Additive Manufacturing: A Review of Mechanical Properties (Postprint), (2016). https://apps.dtic.mil/sti/citations/AD1035268 (accessed August 14, 2022).

[11] S. Malakooti, A.B.M.S. Ud Doulah, Y. Ren, V.N. Kulkarni, R.U. Soni, V.A. Edlabadkar, R. Zhang, S.L. Vivod, C. Sotiriou-Leventis, N. Leventis, H. Lu, Meta-Aerogels: Auxetic Shape-Memory Polyurethane Aerogels, ACS Applied Polymer Materials. 3 (2021) 5727–5738. https://doi.org/10.1021/ACSAPM.1C00987/ASSET/IMAGES/LARGE/AP1C00987_0007.JPEG.

[12] M.I. Hatamleh, C.A. Barrios, Y. Ren, R. Zhang, V.V. Nambiar, A. Williams, P. Shah, A. Guyan, B. Lund, H. Lu, W. Voit, Structural response of 3D-printed rubber lattice structures under compressive fatigue, MRS Communications. 11 (2021) 168–172. https://doi.org/10.1557/S43579-021-00012-4/FIGURES/3.

[13] R. Zhang, H. Chen, S. Malakooti, S. Oman, B. Wang, H. Lu, H. Luo, Quasi-Static and Dynamic Confined Compressive Behavior of Glass Beads by In-Situ X-Ray Micro-Computed Tomography, ASME International Mechanical Engineering Congress and Exposition, Proceedings (IMECE). 12 (2021). https://doi.org/10.1115/IMECE2020-23399.

[14] Q. Guo, C. Zhao, L.I. Escano, Z. Young, L. Xiong, K. Fezzaa, W. Everhart, B. Brown, T. Sun, L. Chen, Transient dynamics of powder spattering in laser powder bed fusion additive manufacturing process revealed by in-situ high-speed high-energy x-ray imaging, Acta Materialia. 151 (2018) 169–180. https://doi.org/10.1016/J.ACTAMAT.2018.03.036.

[15] B. Zhang, S. Liu, Y.C. Shin, In-Process monitoring of porosity during laser additive manufacturing process, Additive Manufacturing. 28 (2019) 497–505. https://doi.org/10.1016/J.ADDMA.2019.05.030.